

Stealth dark matter spectrum using LapH and Irreps

R. C. Brower,¹ C. Culver^{1b},² K. K. Cushman^{1b},^{3,*} G. T. Fleming^{1b},^{3,4} A. Hasenfratz^{1b},⁵ D. Howarth^{1b},⁶ J. Ingoldby^{1b},^{7,8} X. Y. Jin^{1b},⁹ G.D. Kribs^{1b},¹⁰ A. S. Meyer^{1b},¹¹ E. T. Neil^{1b},⁵ J. C. Osborn^{1b},⁹ E. Owen^{1b},¹ S. Park^{1b},^{11,12} C. Rebbi^{1b},¹ E. Rinaldi^{1b},¹³ D. Schaich^{1b},² P. Vranas^{1b},^{11,12} E. Weinberg^{1b},^{1,14} and O. Witzel^{1b}¹⁵

(Lattice Strong Dynamics (LSD) Collaboration)

¹*Department of Physics and Center for Computational Science,
Boston University, Boston, Massachusetts 02215, USA*

²*Department of Mathematical Sciences, University of Liverpool, Liverpool L69 7ZL, UK*

³*Department of Physics, Sloane Laboratory, Yale University, New Haven, Connecticut 06520, USA*

⁴*Theoretical Physics Division, Fermilab, Batavia, IL 60510, USA*

⁵*Department of Physics, University of Colorado, Boulder, Colorado 80309, USA*

⁶*Physics Division, Lawrence Berkeley National Laboratory, Berkeley, California 94720, USA*

⁷*Abdus Salam International Centre for Theoretical Physics, Strada Costiera 11, 34151, Trieste, Italy*

⁸*Institute for Particle Physics Phenomenology, Durham University, Durham DH1 3LE, UK*

⁹*Computational Science Division, Argonne National Laboratory, Argonne, Illinois 60439, USA*

¹⁰*Institute for Fundamental Science and Department of Physics,
University of Oregon, Eugene, Oregon 97403, USA*

¹¹*Physical and Life Sciences Division, Lawrence Livermore National Laboratory, Livermore, California 94550, USA*

¹²*Nuclear Science Division, Lawrence Berkeley National Laboratory, Berkeley, California 94720, USA*

¹³*Interdisciplinary Theoretical and Mathematical Sciences Program (iTHEMS),
RIKEN, 2-1 Hirosawa, Wako, Saitama 351-0198, Japan*

¹⁴*NVIDIA Corporation, Santa Clara, California 95050, USA*

¹⁵*Center for Particle Physics Siegen (CPPS), Theoretische Physik 1,
Naturwissenschaftlich-Technische Fakultät, Universität Siegen, 57068 Siegen, Germany*

We present non-perturbative lattice calculations of the low-lying meson and baryon spectrum of the SU(4) gauge theory with fundamental fermion constituents. This theory is one instance of stealth dark matter, a class of strongly coupled theories, where the lowest mass stable baryon is the dark matter candidate. This work constitutes the first milestone in the program to study stealth dark matter self-interactions. Here, we focus on reducing excited state contamination in the single baryon channel by applying the Laplacian Heaviside method, as well as projecting our baryon operators onto the irreducible representations of the octahedral group. We compare our resulting spectrum to previous work involving Gaussian smeared non-projected operators and find good agreement with reduced statistical uncertainties. We also present the spectrum of the low-lying odd-parity baryons for the first time.

I. INTRODUCTION

Dark matter makes up about 84% of the mass of the Universe, but its composition remains a mystery. Given that around 99% of the mass of visible matter in the Universe arises from the strong dynamics of quantum chromodynamics (QCD), it is well motivated to consider dark matter candidates whose mass arises from the dynamics of some new confining gauge theory. For reviews, see Refs. [1–3]. There are a large variety of theories that can lead to viable dark matter as dark baryons, for instance see Refs. [4–15].

In this paper, we focus on stealth dark matter [9], where the Standard Model is extended to include an SU(4) gauge theory with four fermions in the fundamental representation that produces a spectrum of composite particles. The lightest dark baryon is stable, electrically neutral, and provides a viable candidate for the dark matter in the Universe. Previous lattice studies of

stealth dark matter have investigated the effective Higgs coupling [7, 9], the dark baryon electromagnetic polarizability [16], and the confinement transition and its relation to gravitational waves [17–19]. We have recently [20] been working to extend this research program to include studies of stealth dark matter self-interactions, which is the motivation of the work presented here. In the following we refer to stealth dark matter as the SU(4) gauge theory which we study in the quenched limit with two fundamental flavors in the valence sector.

In order to study stealth dark matter self-interactions from first principles, Lüscher’s method [21, 22] can be applied to non-perturbative lattice calculations of the single- and two-baryon spectrum. Such analyses require high precision energy measurements from multi-baryon correlation functions, which still present challenges to the lattice community in studies of QCD [23–25]. Stealth dark matter with four colors represents a more challenging problem compared to QCD due to the larger number of fermion Wick contractions required to compute baryon correlation functions, as well as the reduced signal-to-noise ratio. On the other hand, the physical parameter space for stealth dark matter extends to much heavier

* kimmy.cushman@yale.edu

pion-to-nucleon mass ratios than for QCD at the physical point, which ameliorates some of the challenges related to studying baryons.

As a first step towards study of baryon interactions, we begin in this work by computing baryon masses using state of the art lattice QCD techniques. To achieve the greatest signal in our SU(4) hadron correlation functions, we implement traditional and stochastic Laplacian Heaviside (LapH) smearing (also known as distillation) [26, 27]. We also project our operators into irreducible representations (irreps) of the lattice octahedral group [28], as is done in state-of-the-art hadron-scattering studies of QCD [25, 29–31]. This paper represents the first application of both LapH and irrep projection on the meson and baryon spectrum of stealth dark matter.

In this work, we analyze the spectrum of the SU(4) gauge theory with fundamental fermions in the quenched approximation. We consider the isospin symmetric limit of two-flavor mesons and baryons. We study three quenched ensembles with volume $32^3 \times 64$ and $\beta = 11.028, 11.5, \text{ and } 12.0$. We estimate the ground state and first-excited state energies of the pseudoscalar meson, the vector meson, and irrep projected even- and odd-parity spin-0, spin-1, and spin-2 baryons with 2-point correlation functions of LapH smeared operators. We use a simple operator basis to perform a combined fit analysis, and we apply model averaging [32, 33] to all of our fits. We then compare our ground state energy values to the results presented in an initial study of the SU(4) stealth dark matter spectrum involving simpler operators [7].

This paper is organized as follows: in Section II we describe our operator optimization, with Section II A describing how operators are projected onto the irreducible representations of the octahedral group, and then Section II B reviewing the Laplacian Heaviside method and describing our implementation. In Section III, we describe our operator basis and fitting procedure, and compare our spectrum results to results from Ref. [7]. We present our conclusions in Section IV.

II. OPTIMIZING OPERATORS

In this section, we develop the framework for the operator construction we use for the baryon scattering problem needed to study stealth dark matter self interactions. We anticipate the scattering problem to present challenges. The first is the statistical challenge due to the exponentially decreasing signal-to-noise ratio at large Euclidean times, which is expected to scale like $e^{-2m_{\text{PS}}t}$ for SU(4) as opposed $e^{-\frac{3}{2}m_{\text{PS}}t}$ for SU(3) [34–36], where m_{PS} is the mass of the pseudoscalar meson. In addition, we eventually will need to construct a large variational basis to improve our estimation of the ground state of the one- and two-baryon systems. Completing these calculations for various scattering momenta to access higher-wave scattering channels presents the additional challenge of esti-

imating the all-to-all propagator. The following sections discuss how projecting onto lattice irreps and implementing the LapH method address these challenges.

One way of improving the signal in our correlation functions is to project operators into the irreps of the octahedral group. By using a set of operators in a definite irrep, we reduce the contamination in our signal from states with different spin.

Another way is using the LapH method [26], which has three important benefits. First, it provides a low-rank approximation to the all-to-all propagator. Second, LapH has been shown to reduce excited state contamination in correlation functions [20, 26, 27]. This is important for scattering measurements because Lüscher’s method requires analyzing energy differences, and we need the largest signal-to-noise ratio possible. Finally, LapH allows for great flexibility and computational efficiency in the construction of a large variational basis of operators.

All operators presented in this work are defined with all fermion fields at a single point prior to LapH smearing. We do not include operators with displacement or nonzero momentum in this work.

A. Projection onto irreducible representations

In this section, we first review the motivation for using lattice irreps in Section II A 1. In Section II A 2 we set up our notation and describe our choice of flavor wave functions, contrasting our SU(4) gauge theory choices against what would be done for SU(3). Then in Section II A 3, we review the algorithm for constructing irreps and describe our basis choice. The results of our irrep projections are presented in the Appendix in Table X.

1. Irreps and SU(4)

When a continuum field theory is discretized onto a lattice, the symmetry group SO(3) of rotations is broken. Instead of the continuous rotations of the sphere, a cubic lattice has symmetries of the octahedral group, O , describing all of the discrete rotations about the axes of symmetry of the cube. In the case of fermion representations with positive and negative parity, we are concerned with the breaking of O(3) into the 96-element double point group, O_h^D [28]. In the continuum, there are infinitely many spin irreps of O(3), defined by the quantum numbers J and P , where $J = 0, \frac{1}{2}, 1, \frac{3}{2}, 2, \frac{5}{2}, 3, \frac{7}{2}, \dots$, and $P = \pm 1$. However for a lattice field where we consider the double point group symmetries, there are just 16 irreps, $G_{1g}, G_{1u}, G_{2g}, G_{2u}, H_g, H_u$ for fermions, and $A_{1g}, A_{1u}, A_{2g}, A_{2u}, E_g, E_u, T_{1g}, T_{1u}, T_{2g}, T_{2u}$ for bosons, where the subscripts g and u denote positive and negative parity, respectfully.

Due to the broken symmetry on the lattice, we cannot construct hadronic operators with definite quantum number J . We can only project operators into definite

J	Λ	J	Λ
0	A_1	$\frac{1}{2}$	G_1
1	T_1	$\frac{3}{2}$	H
2	$E \oplus T_2$	$\frac{5}{2}$	$G_2 \oplus H$
3	$A_2 \oplus T_1 \oplus T_2$	$\frac{7}{2}$	$G_1 \oplus G_2 \oplus H$
4	$A_1 \oplus E \oplus T_1 \oplus T_2$	$\frac{9}{2}$	$G_1 \oplus 2H$

TABLE I: Subduction tables for the five lowest integer (left) and half-integer (right) spin representations, J , into octahedral group representations, Λ .

lattice irreps. The discretization forces a *subduction* of spin irreps into lattice irreps. In the continuum limit, when the full symmetry is restored, the lattice irreps are induced back to the spin irreps. We use the subduction rules, as given in Table I, to select operators of interest and interpret the spectrum.

In the study of SU(4) gauge theory, we are only interested in bosonic representations due to the even number of colors, so we will only be dealing with positive- and negative-parity operators in the A_1, A_2, E, T_1, T_2 irreps. One can find detailed presentations of fermionic representations in Refs. [37, 38].

To reiterate, our baryon operators are bosons, and the only quantum numbers we care about are IJ^P , rather than IGJ^{PC} as one would consider for mesons. In this work we will only consider operators with zero orbital angular momentum, so $J = S$, with a maximum value of $S = 2$. Hence, we only need the first three rows of the left-side table in Table I. The irrep projection provides the J^P quantum numbers and, as we describe in the next section, we perform a separate projection onto isospin I as well. Note that in this work, we focus on constructing two-flavor baryons. Hence, isospin, I , is a sufficient quantum number to describe the flavor content of our baryons (as opposed to also keeping track of stealth dark matter analogues of strangeness, charm, etc.).

According to the subduction table, to study the spin-0 baryon that is the dark matter candidate, we construct operators in the A_1 irrep. The next particle in the spectrum that overlaps with the A_1 irrep has spin 4. Hence, correlation functions constructed from the A_1 irrep have no excited state contamination from physical states with spin 1 or spin 2, improving our signal compared to non-projected operators. We also study the spectrum associated with $S = 1$ through projections onto T_1 , as well as $S = 2$, through projections onto E and T_2 .

2. Setup for constructing irreps

To see how the irreps are constructed, first consider an SU(4) baryon operator, \mathcal{O} , to be given by

$$\mathcal{O} = \sum_{\substack{c_1 c_2 c_3 c_4 \\ f_1 f_2 f_3 f_4 \\ \alpha_1 \alpha_2 \alpha_3 \alpha_4}} \psi_{c_1 f_1 \alpha_1} \psi_{c_2 f_2 \alpha_2} \psi_{c_3 f_3 \alpha_3} \psi_{c_4 f_4 \alpha_4} \times \epsilon^{c_1 c_2 c_3 c_4} \phi^{f_1 f_2 f_3 f_4} \chi^{\alpha_1 \alpha_2 \alpha_3 \alpha_4}, \quad (1)$$

where ψ are Grassmann numbers indexed with color indices, c_i , flavor indices, f_i , and spin indices, α_i . The Grassmann numbers are contracted with three rank-4 tensors. These tensors are the Levi-Civita tensor, ϵ , the flavor wavefunction, ϕ , and the spin projection, χ . We use this notation for convenience, but also to emphasize the symmetry constraints imposed by the Grassmann numbers, as described below. Note that for non-local operators, the Grassmann numbers would also need to be contracted with some position/displacement tensor involving gauge links. In this work, we are considering only local operators so we omit the position tensor. Here, our goal is to find ϕ and χ such that the operators have definite isospin and lattice irrep.

In the sections below, we compare our SU(4) spectrum results to Ref. [7], where operators are constructed using “di-quark” operators given by

$$\mathcal{O} = \left(\psi_1^\alpha X_1^{\alpha\beta} \psi_2^\beta \right) \left(\psi_3^\sigma X_2^{\sigma\delta} \psi_4^\delta \right), \quad (2)$$

with ψ_i representing fermions with two flavors labeled u and d . The rank-2 spin tensors X_1 and X_2 are identified with spin according to

$$\text{spin-0} : X_1 = C\gamma_5, X_2 = C\gamma_5 \quad (3)$$

$$\text{spin-1} : X_1 = C\gamma_i, X_2 = C\gamma_5, i = 1, 2, 3 \quad (4)$$

$$\text{spin-2} : X_1 = C\gamma_i, X_2 = C\gamma_j, i \neq j \quad (5)$$

where $C = \gamma_4\gamma_2$ is a charge-conjugation operator. As an example, their spin-0 operator,

$$\mathcal{O} = \left(u^\alpha (C\gamma_5)^{\alpha\beta} d^\beta \right) \left(u^\sigma (C\gamma_5)^{\sigma\delta} d^\delta \right), \quad (6)$$

in our notation corresponds to

$$\chi^{\alpha\beta\sigma\delta} = (C\gamma_5)^{\alpha\beta} (C\gamma_5)^{\sigma\delta} \quad (7)$$

$$\phi^{f_1 f_2 f_3 f_4} = \begin{cases} 1 & \text{for } (f_1, f_2, f_3, f_4) = (u, d, u, d) \\ 0 & \text{otherwise.} \end{cases} \quad (8)$$

Note that these operator do not have definite total isospin and spin.

To construct our irrep projected operators in this work, we use the fact Grassmann numbers anticommute, so when they are contracted with tensors to form a scalar, as in Equation 1, only the *totally anti-symmetric* part of the product $\epsilon\phi\chi$ will contribute. Given that the color

tensor, ϵ , is totally antisymmetric, only the totally symmetric part of the product of the flavor and spin tensors contributes.

To construct two-flavor baryon operators in $SU(4)$ (gauge theory), we can gain insight by looking at the totally symmetric spin-flavor irreps of $SU_{S,F}(4) \supset SU_S(2) \times SU_F(2)$, with S denoting non-relativistic 2-component spin, and F denoting flavor. That is, we can embed representations of $SU_S(2) \times SU_F(2)$ into representations of $SU_{S,F}(4)$, where a representation of the spin-flavor group has a spin label and a flavor label. The totally symmetric spin-flavor wave function can be decomposed using the Young diagrams below:

$$\begin{array}{c}
 \begin{array}{|c|c|c|c|} \hline \square & \square & \square & \square \\ \hline \end{array} \\
 \text{\scriptsize } SU_{S,F}(4) \\
 = \\
 \begin{array}{|c|c|c|c|} \hline \square & \square & \square & \square \\ \hline \end{array} \times \begin{array}{|c|c|c|c|} \hline \square & \square & \square & \square \\ \hline \end{array} \\
 \text{\scriptsize } SU_S(2) \quad \text{\scriptsize } SU_F(2) \\
 + \\
 \begin{array}{|c|c|c|} \hline \square & \square & \square \\ \hline \square & & \\ \hline \end{array} \times \begin{array}{|c|c|c|} \hline \square & \square & \square \\ \hline \square & & \\ \hline \end{array} \\
 \text{\scriptsize } SU_S(2) \quad \text{\scriptsize } SU_F(2) \\
 + \\
 \begin{array}{|c|c|} \hline \square & \square \\ \hline \square & \square \\ \hline \end{array} \times \begin{array}{|c|c|} \hline \square & \square \\ \hline \square & \square \\ \hline \end{array} . \\
 \text{\scriptsize } SU_S(2) \quad \text{\scriptsize } SU_F(2)
 \end{array} \quad (9)$$

This equation tells us that a totally symmetric spin-flavor wavefunction (horizontal Young Diagram on the left-hand side) can be decomposed into a product of spin and flavor wavefunctions in three ways. The first term represents $S = 2, I = 2$. The second term represents $S = 1, I = 1$. And the third term represents $S = 0, I = 0$.

The analogous equation for $SU(3)$ gauge theory is

$$\begin{array}{c}
 \begin{array}{|c|c|c|} \hline \square & \square & \square \\ \hline \end{array} \\
 \text{\scriptsize } SU_{S,F}(4) \\
 = \\
 \begin{array}{|c|c|c|} \hline \square & \square & \square \\ \hline \end{array} \times \begin{array}{|c|c|c|} \hline \square & \square & \square \\ \hline \end{array} \\
 \text{\scriptsize } SU_S(2) \quad \text{\scriptsize } SU_F(2) \\
 + \\
 \begin{array}{|c|c|} \hline \square & \square \\ \hline \square & \\ \hline \end{array} \times \begin{array}{|c|c|} \hline \square & \square \\ \hline \square & \\ \hline \end{array} . \\
 \text{\scriptsize } SU_S(2) \quad \text{\scriptsize } SU_F(2)
 \end{array} \quad (10)$$

The first term, with totally symmetric isospin and spin corresponds to the Δ baryon, which has $I = S = 3/2$. The second term corresponds to the nucleon, with $I = S = 1/2$.

The relativistic Dirac spins can have more non-vanishing contributions, but in this work, we focus on the operators with $S = I$. We assume that, as in QCD, the spectrum can be described by a constituent quark model, where the baryons with $S \neq I$ require orbital angular momentum and have higher masses. Using these symmetries to determine the correct combination of lattice irreps and isospins, we construct three sets of spin-flavor wavefunctions: A_1 with $I = 0$, T_1 with $I = 1$, and T_2 and E_g with $I = 2$. The flavor wavefunctions with definite $I = 0, 1, 2$ are determined from the $SU(2)$ Clebsch-Gordon coefficients, and are given in the Appendix in Table IX.

Given a particular flavor wavefunction, we can write Equation 1 in a more familiar form by combining the flavor tensor with the Grassmann fields and labeling the

quarks by their flavor. For example, the operator with the $I = 0$ flavor wavefunction labeled $MS_0^{(2)}$ in Table IX, $(ud - du)(ud - du)$, can be written as

$$\mathcal{O}^\Lambda = \epsilon^{abcd} (u_\alpha^a d_\beta^b - d_\alpha^a u_\beta^b) (u_\sigma^c d_\delta^d - d_\sigma^c u_\delta^d) \chi_{\alpha\beta\sigma\delta}^\Lambda, \quad (11)$$

where Λ indicates the lattice irrep, and χ^Λ is the spin tensor wavefunction for that irrep. Below, we summarize what is needed to understand our application of the irrep projected spin tensors, χ^Λ , listed in Table X.

3. Projecting into a definite irrep

Here we use the usual irrep projection formula [29], as reviewed in Appendix A 5. For each irrep Λ , we produce $d_\Lambda \times K$ unique operators, $\chi^{\Lambda\lambda,k}$, $\lambda = 1, \dots, d_\Lambda$, $k = 1, \dots, K$. Here, d_Λ is the dimension of the irrep, and K is the number of copies in the irrep.

By the definition of being an irrep, each of the K sets of d_Λ operators is a closed subspace under application of all elements of the group of lattice rotations. Therefore, once $\chi^{\Lambda\lambda,k}$ is calculated for each λ , we are free to choose a basis in the d_Λ dimensional subspace defined by each irrep. In this work, we compute the spin projections using Equation A2, and then perform the basis transformation which diagonalizes the group element corresponding to rotation of $\pi/2$ about the z -axis, C_{4z} . For example, $d_\Lambda = 2$ for the E_g irrep, so the matrix representation of C_{4z} is 2×2 . It has eigenvalues $R_z = \{-1, 1\}$. These rotation group eigenvalues correspond to S_z eigenvalues in the Lie algebra $\mathfrak{su}(2)$ according to

$$R_z = e^{i\pi/2 S_z}. \quad (12)$$

In the E_g example, $S_z = \{0, 2\}$. The other positive-parity irrep corresponding to spin-2 is T_{2g} , which has algebra eigenvalues $S_z = \{-1, 1, 2\}$. Thus, these two irreps span the full spectrum of spin-2, with $S_z = \{-2, -1, 0, 1, 2\}$.¹

The diagonalized irrep-projected spin tensors for irreps $A_{1g}, E_g, T_{1g}, T_{2g}$ and A_{1u}, E_u, T_{1u} , and T_{2u} are tabulated in Table X. As a result of the diagonalization, S_z are used as a label for the irrep row instead of λ .

B. Laplacian Heaviside method (LapH)

The basic concept of LapH is to construct correlation functions from a low rank approximation of the all-to-all propagator by using the low modes of the gauge invariant Laplacian [26]. In this section, we first review the formalism of LapH, and then discuss our operator construction through a baryon correlation function example. We then discuss LapH in practice, with a discussion about optimization and timing.

¹ Note that $-1 = e^{i\pi/2 \cdot -2} = e^{i\pi/2 \cdot 2}$, so $R_z = -1$ appearing in both E_g and T_{2g} allows for both $S_z = 2$ and $S_z = -2$ as required.

1. LapH formalism

LapH is essentially a form of quark field smearing. The source and sink quark fields, ψ , at spacetime position (x, t) are smeared according to

$$\psi_\alpha^a(x, t) \rightarrow \sum_{i=1}^{N_{\text{vec}}} V_{x,a|i}(t) V_{i|y,b}^\dagger(t) \psi_\alpha^b(y, t), \quad (13)$$

where color indices are given by Latin letters, a, b, \dots and Dirac spinor indices are given by Greek letters, α, β, \dots . Above, Einstein summation convention is used for the sum over spatial position y and color index b , but the sum over eigenvectors is written explicitly to draw attention to the fact that the sum only runs up to the chosen parameter N_{vec} . The matrices V are the eigenvectors of the gauge invariant lattice Laplacian, Δ , given by

$$\Delta_{xy}^{ab}(t) = \sum_{k=1}^{N_d-1} \left(U_k^{ab}(x, t) \delta_{y, x+\hat{k}} + (U^\dagger)_k^{ab}(y, t) \delta_{y, x-\hat{k}} \right) - 2\delta_{xy} \delta_{ab} \quad (14)$$

$$\Delta_{xy}^{ab}(t) V_{x,a|i}(t) = \lambda_i(t) V_{y,b|i}(t), \quad (15)$$

where $N_d - 1$ is the number of spatial dimensions, and U_k are the gauge link fields in direction k . By ordering the eigenvectors by increasing magnitude of their eigenvalues, λ_i , the smearing, Equation 13, becomes a sum over the first N_{vec} low modes of the Laplacian. These are analogous to the low Fourier modes in a scalar field theory. In the limit $N_{\text{vec}} \rightarrow N_{\text{vec}}^{(\text{max})} = L_x^3 N_c$, the smearing operation becomes the identity, and the quark field is not smeared, i.e. $\psi(x, t) \rightarrow \psi(x, t)$. In the limit $N_{\text{vec}} \rightarrow 0$, the quark field is smeared to a wall source.

Computationally, we compute N_{vec} eigenvectors, V , and solve for the propagator, D^{-1} , using the eigenvectors as the source, and then contracting the result with the Hermitian conjugate of each eigenvector at the sink. The resulting object is the perambulator, τ , defined as

$$\tau_{i_0}^{\alpha\alpha_0}(t, t_0) = V_{i|x}^\dagger(t) D_{\alpha\alpha_0}^{-1}(x, t|x_0, t_0) V_{x_0|i_0}(t_0), \quad (16)$$

which can be interpreted as the matrix of N_{vec}^2 *eigenvector-to-eigenvector* propagators (in contrast to point-to-all or all-to-all propagators). The eigenvectors and perambulators are then saved to disk and, depending on how they are contracted with spin-tensors, can be used to form any number of hadron operators. This is true even with displacements and projections onto different momenta, as described in Ref. [26]. Therefore, the ability to construct a large variational basis with the same initial building blocks of eigenvectors and perambulators makes up for the greater complexity of implementing LapH.

2. Example correlation functions using LapH

The operator and correlation function construction using LapH is nearly the same for SU(3) and SU(4) mesons, the only difference being the number of color indices carried on the eigenvectors. See for example Ref. [26] or Ref. [20].

Here, we show the application of LapH to the baryon example shown in Equation 11. Suppressing the spatial, temporal, and color indices for clarity, the correlation function without LapH is given by

$$\begin{aligned} C(x, x') &= \epsilon \left(u_\alpha d_\beta - d_\alpha u_\beta \right) (u_\sigma d_\delta - d_\sigma u_\delta) \chi_{\alpha\beta\sigma\delta} \\ &\times \epsilon \left(\bar{u}_{\alpha'} \bar{d}_{\beta'} - \bar{d}_{\alpha'} \bar{u}_{\beta'} \right) \left(\bar{u}_{\sigma'} \bar{d}_{\delta'} - \bar{d}_{\sigma'} \bar{u}_{\delta'} \right) \tilde{\chi}_{\alpha'\beta'\sigma'\delta'} \\ &= \epsilon^{abcd} \epsilon^{a'b'c'd'} \chi_{\alpha\beta\sigma\delta} \tilde{\chi}_{\alpha'\beta'\sigma'\delta'} \\ &\times \left(D_{aa'}^{-1} D_{cc'}^{-1} - D_{ac'}^{-1} D_{ca'}^{-1} \right) \\ &\times \left(D_{\beta\beta'}^{-1} D_{\delta\delta'}^{-1} - D_{\beta\delta'}^{-1} D_{\delta\beta'}^{-1} \right) \end{aligned} \quad (17)$$

where $\tilde{\chi}_{\alpha\beta\sigma\delta} = \chi_{\alpha'\beta'\sigma'\delta'}^* \gamma_4^{\alpha\alpha'} \gamma_4^{\beta\beta'} \gamma_4^{\sigma\sigma'} \gamma_4^{\delta\delta'}$, as required to compute \mathcal{O}^\dagger . Now, applying LapH, and writing the color indices explicitly, the correlation function becomes

$$\begin{aligned} C(x, x_0) &= \epsilon^{abcd} \epsilon^{a'b'c'd'} \chi_{\alpha\beta\sigma\delta} \tilde{\chi}_{\alpha'\beta'\sigma'\delta'} \sum_{i,j,k,l}^{N_{\text{vec}}} T_{ijkl} T_{i'j'k'l'}^\dagger \\ &\times \left(\tau_{ii'}^{\alpha\alpha'} \tau_{kk'}^{\sigma\sigma'} - \tau_{ik'}^{\alpha\sigma'} \tau_{ki'}^{\sigma\alpha'} \right) \left(\tau_{jj'}^{\beta\beta'} \tau_{ll'}^{\delta\delta'} - \tau_{jl'}^{\beta\delta'} \tau_{\delta j'}^{\beta\delta'} \right), \end{aligned} \quad (19)$$

where

$$T_{ijkl} = V_{a|i} V_{b|j} V_{c|k} V_{d|l}, \quad (20)$$

$$T_{ijkl}^\dagger = V_{i|a}^\dagger V_{j|b}^\dagger V_{k|c}^\dagger V_{l|d}^\dagger. \quad (21)$$

As is the case for mesons, the propagator in position and color space is replaced by the perambulator in the LapH subspace defined by the eigenvectors, and then the eigenvectors are used to take this low mode result back to position space. Again, note that the result is similar to that for SU(3) baryon correlation functions, except that there would be three fermion fields being contracted and there would be three indices on the tensors ϵ, T , and χ above.

It is worth mentioning that these examples consider LapH smearing of point-to-point correlation functions, but it is straightforward to consider momentum projection as usual by summing over all spatial positions with weights $e^{ip \cdot x}$.

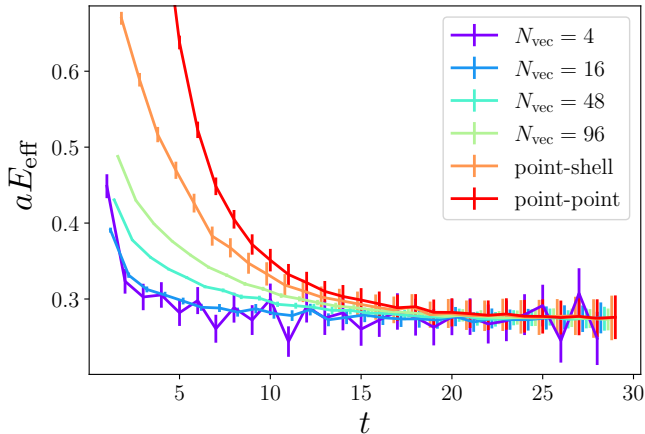


FIG. 1: Hyperbolic cosine form of effective mass of pseudoscalar meson correlation function for $32^3 \times 64$ ensemble of 200 configurations with $\beta = 12$ and $\kappa = 0.1475$. Plot compares different LapH smearing parameters, N_{vec} , to non-LapH point-point and point-shell correlation functions. Lines connecting data points are included to guide the eye.

3. LapH in practice

Using LapH smearing reduces excited state contamination in a similar way as Gaussian smearing, but with LapH, the tunable smearing parameter is N_{vec} . Figure 1 compares the amount of excited state contamination appearing in our SU(4) $\beta = 12$ pseudoscalar meson correlation functions produced with a range of smearing, from no smearing (point-point) to smearing with $N_{\text{vec}} = 4$, the four zero modes of the Laplacian (due to there being four colors), corresponding to a wall source. As expected, the effective mass with the most excited state contamination comes from the point-point correlation function with no smearing, the red, highest curve. By inspection, one can see that the LapH effective masses, the lowest four curves, have significantly less excited state contamination than both the point-point and Gaussian sink smeared point-shell correlation functions.² However, one can see that all of the curves converge to the same effective mass plateau.

Figure 2 shows a closer look at the same LapH effective masses described above, but zoomed in and with the purple $N_{\text{vec}} = 4$ curve lightened for clarity. One can see that while there is less excited state contamination for smaller values of N_{vec} , the errors are larger. Therefore,

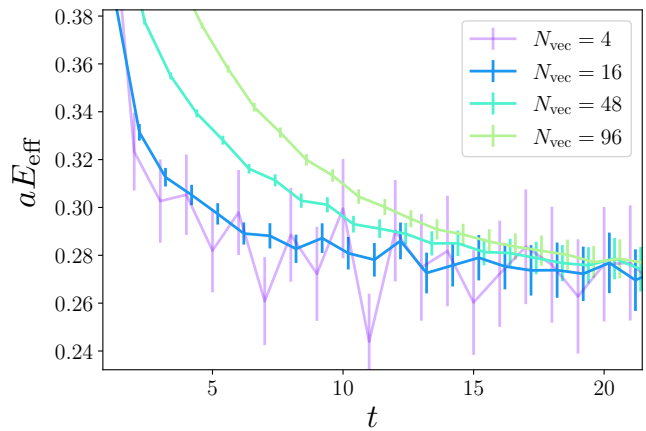


FIG. 2: Zoomed in version of Figure 1, showing only LapH effective masses to compare excited state contamination and relative error. Lines connecting data points are included to guide the eye.

in choosing N_{vec} , one has to consider the trade off between increasing systematic or statistical error.

Given that the parameter N_{vec} controls the overlap of the operator with states in the spectrum, operators constructed with different number of eigenvectors can be used as a variational basis in a generalized eigenvalue problem. In the Section III E below, we follow a different approach and perform combined fits of correlation functions using different numbers of eigenvectors.

Looking back at Equation 19, one can see that the baryon correlation function requires the contraction of $2N_c$ eigenvector indices, running from $1, \dots, N_{\text{vec}}$. More specifically, the leading order of computational complexity in eigenvector indices for Eq. (19) is $O(N_{\text{vec}}^{N_c+1})$. In other words, the computational cost is proportional to $O(N_{\text{vec}}^5)$ for SU(4) baryons; see Appendix A 4 for more details. Therefore, the computational cost of these contractions is especially problematic for baryons in larger gauge groups like SU(4), and will pose a significant challenge for 2-baryon correlation functions which will require $4N_c$ contractions. Similarly, it will require $O(N_{\text{vec}}^{2N_c+1}) = O(N_{\text{vec}}^9)$ of leading complexity for SU(4) baryon-baryon scattering and this is extremely expensive, and therefore it will be essential to apply the stochastic LapH (sLapH) method which is discussed in the next section. For the single-baryon correlation functions being studied in this work, we find that the contraction step presented in Equation 19 becomes the leading contribution to the computation time of a baryon correlation function for $N_{\text{vec}} \approx 32$. This number of course depends on algorithmic and hardware details, discussed further in Section IV and Appendix A 4.

² The amount of excited state contamination appearing in the Gaussian smeared data depends on the parameters of the smearing. The non-LapH correlation functions were computed using the Chroma implementation provided by Michael Buchoff [7]. In this work, gauge invariant quark smearing was used with smearing parameters `wvf.param` = 4.0 for $\beta = 11.028, 11.5$ and `wvf.param` = 8.0 for $\beta = 12$.

β	Plaquette	$\sqrt{8t_0}/a$	κ
11.028	0.578791(4)	5.2411(16)	0.1554
11.5	0.605634(3)	7.8707(50)	0.1515
12.0	0.628840(3)	11.550(15)	0.1475

TABLE II: The parameters, plaquette, and Wilson flow scale for each of the three SU(4) $32^3 \times 64$ ensembles considered in this work.

C. Stochastic LapH (sLapH)

sLapH [27] is a powerful method that allows for a significant reduction in the number of vector contractions, while still controlling the number of eigenvectors used to define the LapH subspace and therefore the overlap with different states in the spectrum. Due to the computational cost of computing LapH baryons, we choose to use sLapH when smearing with larger N_{vec} is desired. sLapH vectors, \tilde{V} are defined according to

$$V_{xa|i} \rightarrow \tilde{V}_{xa|n} \equiv \sum_{i=1}^{N_{\text{vec}}} V_{xa|i} \rho_{in}, \quad n = 1, 2, \dots, N_{\text{noise}}, \quad (22)$$

where ρ_{in} is a matrix whose columns are noise vectors. In this work, we use Z_4 noise with interlace- $J = 2$ dilution as defined in Ref. [27]. In the following section, we argue that it is not worth using sLapH for the baryon analysis with our current computational resources. However, it is still useful to use sLapH to study the larger N_{vec} behavior of meson correlation functions to explore the relationship between β and the optimal N_{vec} . This will be essential when we move on to baryon scattering, where the computational cost will be higher as N_{vec} increases, and we will want to maximize the signal at early times due to the exponentially decaying signal-to-noise ratio.

In order to optimize statistical and systematic errors, it is important to consider the relative times required to complete each step of the LapH process. Computational resources and timing are discussed in Appendix A 4.

III. ANALYSIS

A. Ensemble details

In this work, we compute the low-lying meson and baryon spectrum for three quenched SU(4) ensembles with lattice volume $32^3 \times 64$. We use the Wilson gauge action and consider bare lattice couplings $\beta = 11.028, 11.5$ and 12. In Table II we report the corresponding values of the plaquette (normalized to unity) and the Wilson flow scale $\sqrt{8t_0}/a$ (where ‘ a ’ is the lattice spacing) defined through the condition $\{t^2 \langle E(t) \rangle\}_{t=t_0} = 0.4$ [39, 40].

We choose these couplings to match those studied in Ref. [7]. While that earlier work used the heatbath algorithm for gauge configuration generation, here we employ

the hybrid Monte Carlo (HMC) algorithm, in preparation for future work using dynamical fermions. We use a version of the Chroma software system [41], with a force-gradient integrator and a trajectory length of one molecular dynamics time unit (MDTU). Because autocorrelations increase for larger β , we generated 160,000 MDTU for $\beta = 12$ and only around 40,000 MDTU for each of $\beta = 11.028$ and 11.5. For each ensemble we measured observables on 385 thermalized configurations, separating the configurations by 400 MDTU for $\beta = 12$ and by 100 MDTU for the stronger couplings.

For each β we analyze the heaviest valence fermion mass considered by Ref. [7]. We employ Chroma to calculate the perambulators, using the unimproved Wilson fermion action with the values of κ shown in Table II. For the $\beta = 11.028$ and 11.5 ensembles, the corresponding pseudoscalar-to-vector mass ratio is $m_{\text{PS}}/m_V \approx 0.77$. For the $\beta = 12$ ensemble we have heavier valence fermions leading to $m_{\text{PS}}/m_V \approx 0.89$.

B. Fitting details

All of our fits use the same procedure. First, all of our SU(4) meson and baryon operators are bosons and are even under time-reversal, so we ‘fold’ the correlation functions about $N_t/2$ to increase the statistics. Also, all correlation functions are calculated on only one source time. For the case of point-point/point-shell/shell-shell correlations only one measurement is performed, in contrast to ≈ 5 measurements per configuration used in Ref. [7]. This is irrelevant for LapH correlation functions, where $N_{\text{vec}}^{\text{sink}} \times N_{\text{vec}}^{\text{source}}$ measurements are used. Before fitting, we average the correlation functions corresponding to the three polarizations of vector mesons, as well as all S_z components, as listed in Table X, of baryons in the $E, T_1,$ and T_2 irreps.

We perform χ^2 -minimization fits using a full covariance matrix with linear shrinkage [42], as presented in Ref. [43]. We implement model averaging [32, 33] to estimate central values and systematic errors due to the model choices. All correlation functions are fit to hyperbolic cosine models with one, two, and three energy states for a range of fitting regions in Euclidean time. That is, the fit model is

$$\mathcal{C}(t) = \sum_{m=1}^{N_{\text{states}}} a_m \left(e^{-E_m t} + e^{-E_m (N_t - t)} \right), \quad (23)$$

where $N_{\text{states}} = 1, 2, 3$, and the fit parameters are a_m is a real number and E_m is positive. We estimate errors on fit parameters by model averaging errors computed from a sample of parameters obtained using a bootstrap analysis in which we randomly select 385 measurements to form 100 bootstrap samples.

As motivated in Refs. [33, 44] we use strict data quality cuts in our model averaging and only fit to a maximum

time, t_{cut} such that $C(t_{\text{cut}})/C(1)$ is more than eight standard deviations from zero. We also impose quality cuts to determine the models used in the model average. We exclude models where any of the fit parameters are unconstrained, i.e. $\geq 100\%$ error. We also exclude models to more states than the data appear to support.

C. Spectrum comparison with simple operators

In this work, we want to isolate the effects of using LapH and irrep projected operators. Therefore we compare our results to a previous study [7] of the spectrum which does not employ LapH or irrep projected operators. This comparison also serves as a validation of the physics results from our updated simulation code and methods. We ensure our ensembles are statistically compatible with those used in the previous work by fitting correlation functions constructed using the same operators used in the previous work, as described in Equation 2. We choose the Gaussian smearing parameters to match the results of Ref. [7].

Our results of the ground state masses in each channel are obtained by performing a combined fit to three different zero-momentum projected smearing prescriptions: point-point, point-shell, and shell-shell as implemented in Ref. [7]. The same procedure for performing the combined fits is used here as is used for the LapH and irrep projected correlation functions, with more details given in Section III E.

Figure 3 shows the spectrum results in units of the spin-0 baryon. Our results are the data points with error bars and are compared to those quoted in Ref. [7], which are given as the horizontal error bands. We can see that our results are in good agreement with the previous work. Even using the same simple operators at this point, our errors are smaller on average, even though we have less measurements for each channel overall. We attribute this to our more sophisticated analysis procedure, described in Section III B, as well as the fact that we performed a combined fit to the correlation functions with the three smearings.

D. LapH and irrep operator basis

The contractions required to calculate the baryon correlation functions, as in Equation 19, are computationally expensive, and the cost scales badly with the number of LapH eigenvectors, N_{vec} (or noise vectors in the case of sLapH). Therefore, we compute the inexpensive meson correlation functions for a range of N_{vec} in order to study the trade off between reduced excited state contamination and reduced signal. Although the optimization may not transfer directly from the mesons to the baryons, the meson study provides an inexpensive starting point for optimizing the baryon signal.

Figures 1, 2, and 4 show the effective mass of the pseudoscalar meson for the $\beta = 12, 11.028$ and 11.5 ensembles for a range of N_{vec} . The figures show that depending on the coupling, some small N_{vec} choices smear the operator wave function too much to even have a good overlap with the ground state, for example $N_{\text{vec}} = 4$ for $\beta = 12.0$ and $N_{\text{vec}} = 16$ for $\beta = 11.028$. Also varying β has a significant effect on the value of N_{vec} that is large enough such that excited state signal appears at later timeslices, where the fits are performed. For example, excited state signal appears to be significant at $N_{\text{vec}} = 16$ for $\beta = 12.0$ between timeslices $t = 2$ to $t = 8$. On the other hand, the coarsest lattice, with $\beta = 11.028$, for both $N_{\text{vec}} = 32$ and $N_{\text{vec}} = 64$, the signal for excited states diminished by timeslice $t = 8$.

In this work, we focus our computational resources on the even-parity baryons and the pseudoscalar baryon (A_{1u}). We also estimate the rest of the odd-parity spectrum to study the spectrum ordering, using a smaller number of eigenvectors and accepting a larger error for the odd-parity states. Using the initial meson analysis as described above, the number of eigenvectors chosen for the even-parity (and A_{1u}) and odd parity baryon correlation functions, B^+ and B^- are shown in Table III.

β	B^+, A_{1u} N_{vec}	B^- N_{vec}
11.028	32	24
11.5	24	24
11.028	16	16

TABLE III: Number of eigenvectors chosen for baryon correlation functions for each ensemble.

As expected, the coarsest lattice with $\beta = 11.028$ requires the largest number of eigenvectors, $N_{\text{vec}} = 32$, and we are able to get away with using the very small $N_{\text{vec}} = 16$ for the finest lattice with $\beta = 12$.

These choices of N_{vec} are significantly smaller than those used in typical lattice QCD calculations. However, in the baryon spectrum problem here, the bottleneck of the entire lattice calculation is the contractions, so we choose to trade off using a larger number of eigenvectors for increasing statistics. That is, the computational cost is linear in the number of configurations, but it is quartic (or worse) in the number of eigenvectors, so for fixed computational cost, we choose to reduce the number of eigenvectors and increase the number of configurations.

The scaling of the computational cost as a function of the number of (s)LapH vectors also means that using sLapH is not very beneficial with our current computational procedure. While sLapH allows us to increase the number of eigenvectors used for a fixed number of noise vectors, that number of noise vectors has to be sufficiently large to sample the LapH subspace well enough. Therefore, we only use sLapH when constructing the meson correlation functions. This still provides useful information about how the signal varies with N_{vec} and β . The

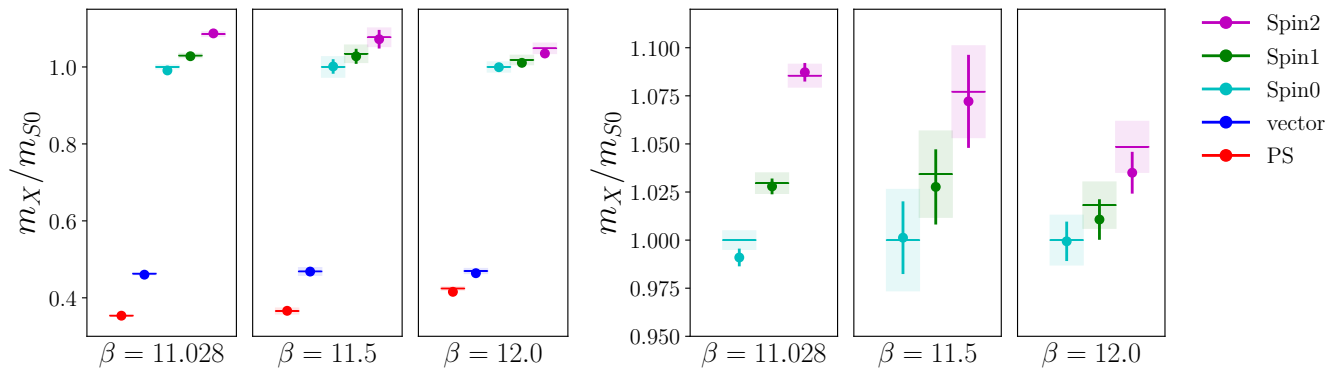


FIG. 3: Spectrum results using the simple operators defined in Equation 2 as used in previous work, Ref. [7]. Our results, colored points with error bars, are compared to the quoted results from the previous work, depicted by error bands. Masses, m_X , are in units of the spin-0 baryon mass, m_{S0} , for each bare coupling, β . The left figure shows all of the states measured in this work, and the right figure shows the same results, zoomed in to focus on the baryons. In the left figure, the errors are smaller than the points.

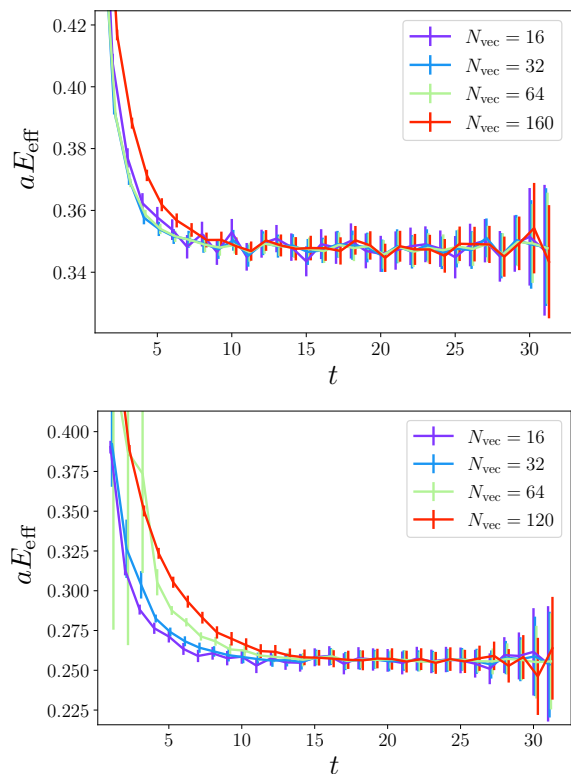


FIG. 4: $\beta = 11.028$ (top) and $\beta = 11.5$ (bottom) pseudoscalar meson effective masses, using the hyperbolic cosine form of the effective mass. Lines connecting data points are included to guide the eye.

LapH smearings used for the mesons are presented in Table IV, with sLapH with $N_{\text{noise}} = 32$ used for $N_{\text{vec}} > 100$.

β	N_{vec}
11.028	16, 32, 64, 160
11.5	16, 32, 64, 120
12.0	8, 16, 32, 64

TABLE IV: Number of eigenvectors chosen for meson correlation functions for each ensemble.

E. Combined Fits

The operators used in this work are zero-momentum, non-displaced operators, and we find that our operators are not orthogonal enough to perform a reliable variational analysis. Instead, for both the baryons and mesons, we perform combined fits to N correlation functions. For the meson analyses, $N = 4$ as four different LapH smearings are used. For the baryon analysis, $N = K$, where K is the total number of copies, indexed by k , for each irrep. The values of K , as tabulated in Table X, are given in Table V.

Λ	K	Λ	K
A_{1g}	4	A_{1u}	2
T_{1g}	5	T_{1u}	4
E_g	3	E_u	2
T_{2g}	3	T_{2u}	2

TABLE V: Number of operators, K , for each irrep, Λ .

We perform a simultaneous χ^2 minimization fit to the N correlation functions, fitting all correlation functions to a model with the same number of states, N_{states} , but allowing the range of timeslices in the fit to vary between the different correlation functions. The fit parameters are

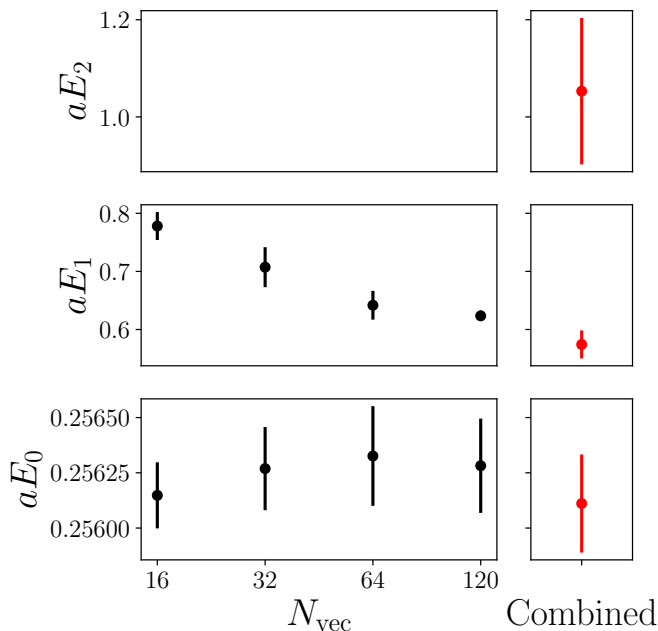


FIG. 5: Results of $\beta = 11.5$ pseudoscalar meson fits with up to two states to single correlation functions constructed with different LapH smearing, N_{vec} (left panel) and combined fits with up to three states to all four correlation functions simultaneously taking into account all data covariances (right panel). Energies given in lattice units.

the N_{states} energy levels, plus the $N \times N_{\text{states}}$ amplitudes of each energy state for each correlation function. We use shrinkage to provide a reliable estimate of the inverse covariance matrix required to perform the χ^2 minimization, taking into account covariances among the data sets used in the combined fit.

1. Meson combined fits varying N_{vec}

For the meson spectrum analysis, we perform combined fits of correlation functions constructed from $N = 4$ different LapH smearings, parametrized by N_{vec} , with operators defined as

$$\mathcal{O}(x, t) = \sum_{ij}^{N_{\text{vec}}} V_{x|i}(t) V_{i|y}^\dagger(t) \bar{u}_\alpha(y, t) \Gamma_{\alpha\beta} \times d_\beta(z, t) V_{z|j}(t) V_{j|x}^\dagger(t), \quad (24)$$

where color indices are suppressed, and $\Gamma = \gamma_5$ for the pseudoscalar meson, and $\Gamma = \gamma_1, \gamma_2, \gamma_3$ for each polarization of the vector meson. As indicated in Section III B, we average over the correlation functions corresponding to the three polarizations of the vector mesons.

Figure 5 shows the fit results after model averaging for the $\beta = 11.5$ pseudoscalar meson ground state and excited state energies in lattice units. The left panel shows

the results of individual fits to each N_{vec} , and the right panel shows the result of a combined χ^2 minimization fit to all four correlation functions simultaneously, which we use as the final results presented in Tables VI, VII, and VIII. Only two-state fits survived model averaging for the single correlation fits, whereas three-state fits contributed to the model average for the combined fit, so a third energy state was extracted. From the single correlation function results in the figure, it is possible to see the effect of increasing N_{vec} , which makes the operator more point-like. For larger N_{vec} , the signal has more overlap with excited states, so the first excited state is better resolved.

Because there is more signal to work with, the combined fit is also able to constrain a third state, which provides better constraints on the lower states. Thus combined fits have the least excited state contamination and are working exactly as desired. By combining the signals of four correlation functions with different overlaps with excited state, it is possible to achieve the best variational estimate of the ground state and first excited state. We found similar results for the mesons for all three ensembles presented here.

2. Baryon combined fits with N_{vec} fixed

For the baryon spectrum analysis, we perform combined fits of the $N = K$ correlation functions defined analogously to the example of Equation 19 with spin-wavefunctions defined in Table X and flavor wavefunctions defined in Table IX, using $I_z = I$. Prior to the analysis, we average the correlation functions corresponding to the different spin-projection of each irrep. From the meson examples, we see that varying N_{vec} in the combined fits can be useful in achieving energy estimates with less excited state contamination. However, due to the high computational cost of increasing the number of eigenvectors for the baryons, we are not able to vary N_{vec} meaningfully enough to achieve correlation functions with significantly different overlaps with higher energy states. We find that varying the operators by using the K different operators resulting from the irrep projection improves the energy estimates even for fixed N_{vec} , as shown in the examples below.

Figure 6 shows an example of single versus combined fit results for the $\beta = 12$ T_{1g} baryon, which corresponds to spin-1. All of the baryon operators, indexed by k , used the same number of eigenvectors, $N_{\text{vec}} = 16$, as shown in Table III. The left panel shows the model averaged fit results to the single correlation functions, and the right panel shows the results of the combined χ^2 minimization to all five correlation functions simultaneously. The single correlation function fits contributing to the model average are two-state fits, whereas the combined fit has enough signal to constrain a third state as well. Although the number of eigenvectors is kept fixed, the operators each have different overlaps with the energy eigenstates.

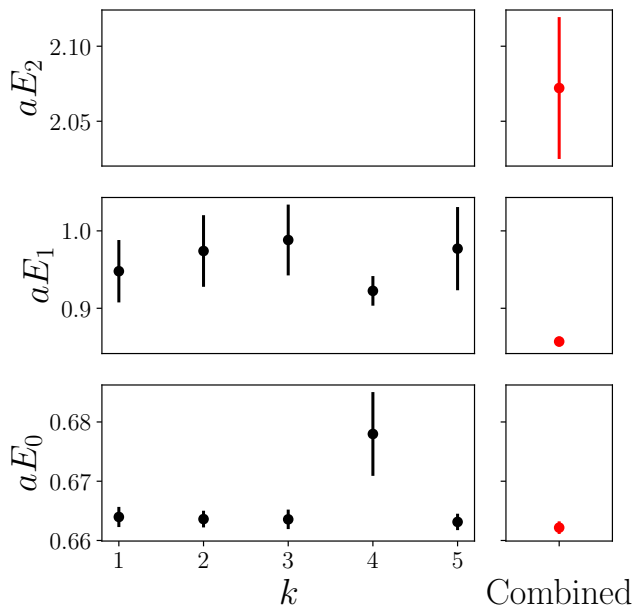


FIG. 6: Results of $\beta = 12$ T_{1g} baryon single fits with up to two states to correlation functions constructed with different operators indexed by k (left panel) and combined fits with up to three states to all five correlation functions simultaneously taking into account all data covariances (right panel). Energies are given in lattice units and some error bars are smaller than the size of the data points.

Here, the most notable example is the $k = 4$ correlation function, which constrains the ground state the least, but gives the lowest estimate of the first excited state with the least error. By combining the signal from all of the correlation functions, the combined fit is able to constrain three states, and provides the best variational estimates of the ground state and first excited state compared to the single correlation function fits. We find that only the $\beta = 12$ baryon combined fits are able to constrain a third state.

Figure 7 shows the fit results to the $\beta = 11.5$ A_{1g} baryon, which corresponds to spin-0. The number of eigenvectors is $N_{\text{vec}} = 24$ for each of the baryon operators, indexed by k . The single correlation function fit results are shown in the left panel, and two examples of combined fit results are shown in the right panel. In this example, both the single fits and combined fits only are able to constrain two energy states. Even so, the final combined fit results, shown as the solid data points in the right panel, have less excited state contamination and smaller uncertainties. This can be understood by looking more closely at the fits which contribute to the model average. We find that the vast majority of the model probability for the single correlation function fits comes from two-state fits starting at timeslice $t = 2$. For the combined fits, models containing timeslice 2 contribute

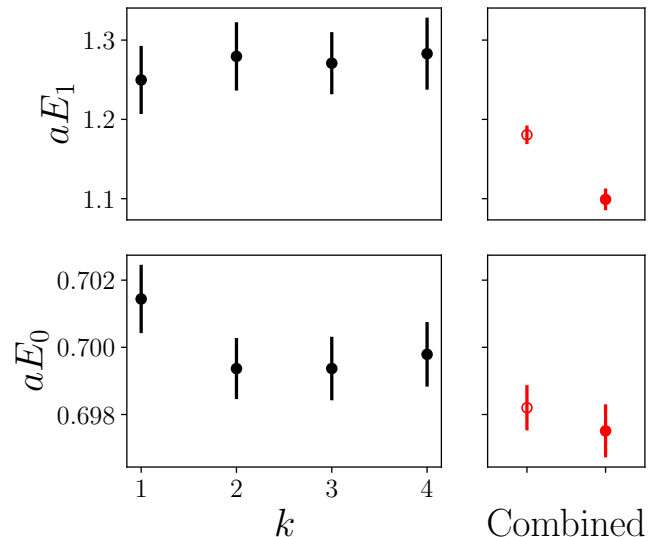


FIG. 7: Results of $\beta = 11.5$ A_{1g} baryon fits to correlation functions constructed with different operators indexed by k are shown in the left panel. The right panel shows two examples of combined fits to all four correlation functions simultaneously, where the difference between the open and closed circles is described in the text. All energies given in lattice units.

very little to the model average ($< 1\%$). However, to provide a direct comparison between the single and combined fits, the combined fit values for the model starting at timeslice $t = 2$ for all correlation functions is shown as the unfilled data points in the right panel. It appears that this combined fit is able to resolve the first excited state with a lower value, indicating that the single correlation function fits have uncontrolled systematic uncertainties. On the other hand, the model with the largest contribution to the combined fit model average is the two-state model with initial timeslices of $t = 3$ for all correlation functions. By combining the signal of the four correlation functions and leveraging the additional statistics, the full combined fit model average is able to constrain an excited state without including timeslice $t = 2$, where there is contamination from higher states. Hence, the final result from the combined fit provide the lowest variational estimate of the ground state and first excited states.

Fits like these, where a third state could not be constrained, occur for all of the $\beta = 11.028$ and $\beta = 11.5$ baryons. We attribute this to the fact that the coarser lattice spacings require larger N_{vec} to achieve a sufficiently localized operator, but we only use $N_{\text{vec}} = 32$ and $N_{\text{vec}} = 24$, respectively. See Appendix A 3 for comments on a few non-intuitive combined fits which required special care.

By studying combined fits for baryon correlation functions, we can see that having a variety of operators leads to a reduced statistical error and reduced excited state

contamination in ground state and first excited state energies. From the meson analysis, we see that varying the number of eigenvectors has a similar effect. Ideally we would use a variety of N_{vec} for each operator, resulting in a large set of operators which could be fit together. However, given the high computational cost of increasing N_{vec} for the baryons, performing combined fits to correlation functions with varying operator construction alone is a robust and relatively inexpensive way to resolve energy states with reduced excited state contamination.

F. Final spectrum results

Tables VI, VII, and VIII show the final results of the ground state, first excited, and second excited state energies in lattice units. Figure 8 shows the full spectra, including our fit results of excited states, for each of the three ensembles, given in units of the A_{1g} ground state mass, which corresponds to the dark matter candidate.

One feature to note is that the positive parity baryons are ordered as in QCD, with increasing spin having a larger mass. That is, we find $m_{A_{1g}} < m_{T_{1g}} < m_{T_{2g}, E_g}$, confirming the ordering found in Ref. [7]. This is an essential feature of stealth dark matter, where the dark matter candidate, the lowest energy stable baryon, must be the scalar. Also of note is the fact that the two irreps corresponding to spin-2, T_{2g} and E_g , are consistent with each other, which indicates that we are not sensitive to the discretization effects which break the symmetry between these two irreps.

Also, as found in Ref. [7], the baryon spectrum is more compressed for the heavier valence fermions used for the $\beta = 12$ ensemble, corresponding to larger $m_{\text{PS}}/m_V \approx 0.89$. This is the behavior expected because the quark mass is a greater contributor to the baryon mass compared to the angular momentum and strong dynamics contributions.

We can confidently state that for all of the ensembles studied in this work, the odd-parity baryons are heavier than the even parity baryons. For the $\beta = 11.028$ and $\beta = 12$ ensembles, the odd-parity spectrum is consistent with an ordering by increasing angular momentum. But for $\beta = 11.5$, we see one three sigma outlier. We find that the $\beta = 11.5$ combined fits to the $K = 2$ A_{1u} , T_{2u} , and E_u correlation functions do not result in a significantly lower ground state, whereas the T_{1u} combined fit to $K = 4$ correlation functions does see a marked improvement. The ground state fit parameters of the T_{1u} individual fits sit right around 0.85, putting the spin-1 mass directly between the spin-0 and spin-2 masses. To fully resolve the spectrum ordering, further study involving more operators or greater statistics are needed.

Figure 9 shows the same results as Figure 8, but compares the results of the mesons and even-parity baryons to the results of the simpler non-LapH Gaussian smeared operators presented in Ref. [7]. Our results from the LapH, irrep projected operators are given by the data

β	11.028	11.5	12.0
PS	0.3477(1)	0.2561(2)	0.2734(2)
vector	0.4527(2)	0.3278(3)	0.3044(3)
A_{1g} (0^+)	0.983(3)	0.6975(8)	0.653(1)
T_{1g} (1^+)	1.012(2)	0.7168(8)	0.662(1)
T_{2g} (2^+)	1.065(4)	0.751(1)	0.678(1)
E_g (2^+)	1.064(3)	0.753(1)	0.677(1)
A_{1u} (0^-)	1.25(1)	0.833(7)	0.732(4)
T_{1u} (1^-)	1.40(4)	0.80(1)	0.733(3)
T_{2u} (2^-)	1.36(7)	0.88(1)	0.756(3)
E_u (2^-)	1.42(3)	0.89(1)	0.755(3)

TABLE VI: Final results of ground state hadron masses in lattice units for the three ensembles studied in this work.

β	11.028	11.5	12.0
PS	0.82(5)	0.57(2)	0.455(7)
vector	0.88(4)	0.60(2)	0.473(5)
A_{1g} (0^+)	1.56(9)	1.10(1)	0.84(1)
T_{1g} (1^+)	1.65(3)	1.094(8)	0.857(6)
T_{2g} (2^+)	1.71(7)	1.19(1)	0.91(3)
E_g (2^+)	1.71(6)	1.20(1)	0.90(3)
A_{1u} (0^-)	2.1(1)	1.30(5)	0.99(6)
T_{1u} (1^-)	n/a	1.12(2)	0.89(2)
T_{2u} (2^-)	2.3(4)	1.4(1)	1.11(4)
E_u (2^-)	n/a	1.5(1)	1.10(4)

TABLE VII: Final results of first excited state hadron masses in lattice units for the three ensembles studied in this work, with “n/a” indicating combined fit not including this excited state.

points with error bars, and the results from the previous work with simpler operators are given by the horizontal error bands. In general, our results with LapH and irrep projected operators have smaller uncertainties and provide estimates of the baryon masses with less excited state contamination. In particular, the $\beta = 12.0$ spectrum presented in the previous work likely suffered from the greatest excited state contamination, yielding the greater discrepancy seen in Figure 9.

IV. CONCLUSION

This work is the first milestone in the research program to calculate stealth dark matter self-interactions using lattice field theory. We presented the first LapH

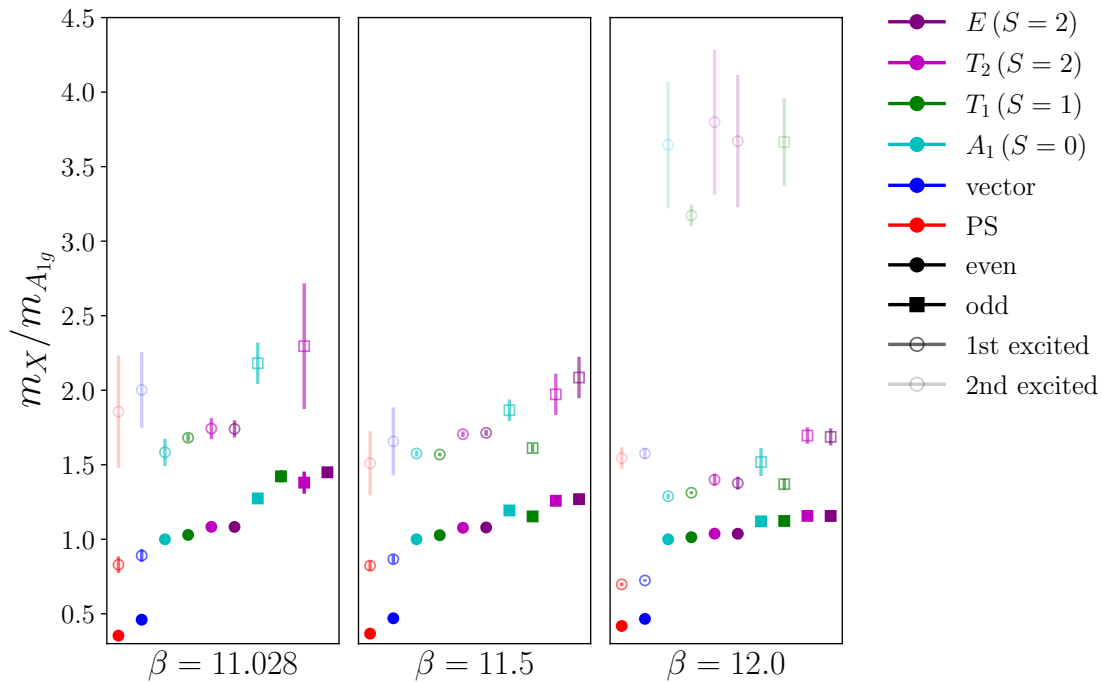


FIG. 8: Final results, including excited states, of combined fits to the LapH smearing and irrep projected correlation functions for the three ensembles studied in this work. All of the results are presented in units of the ground state A_{1g} baryon mass. For each panel, from the left to the right, the first two data points indicate the pseudoscalar and vector mesons. The next four data are for the baryons with even-parity baryons (circles), and the last four data are the odd-parity baryons (squares). Filled and empty symbols are for the ground and 1st excited state masses, respectively. The second excited state masses are presented in a lighter color. Note that the spin label in the legend is meant to aid interpretation; in the continuum limit, the irreps are “injected” to higher spins as well. Also note that some of the data points are larger than the error bars.

smearing, irrep projected results of the baryon spectrum, and presented the first results of the odd-parity baryon spectrum. For three points in the stealth dark matter parameter space, for $N_f = 2$ at three quark masses, we resolved the even-parity baryon ordering with greater precision and reduced systematic error compared to previous work [7] from 2014. However, the changes to the spectrum are small, so the excited state contamination in previous results does not have significant implications on the electromagnetic polarizability results [16] and effective Higgs coupling results [7, 9] found in previous work.

Due to the improved operator construction and use of advanced analysis techniques, including model averaging [32, 33] and shrinkage [42, 43], we achieved ground state precision of 0.1% to 0.3% in the even parity sector, and 0.4% to 5% in the odd parity sector. We also were able to extract first excited state energy estimates for 22 of the 24 baryons, with second excited state energy estimates as well for five baryons.

The baryon-baryon scattering problem required to study stealth dark matter self-interactions will necessitate further developments in the baryon construction and analysis procedure. Having developed SU(4) irreps and

LapH, some interesting paths forward are now open. For example, we may want to include irrep projected displaced quark baryon operators and compute two-baryon systems with finite orbital angular momentum. These constructions would provide a large variational basis of operators that we can use to solve a generalized eigenvalue problem, as is done in state-of-the-art hadron scattering calculations in QCD [25, 30, 31, 45].

As we scale up to solving the baryon-baryon scattering problem, we need to address the issue of the N_{vec} scaling of the computational cost by using sLapH. In addition, implementation of common subexpression elimination [46] would greatly reduce the number of diagrams required to complete Wick contractions required for two-baryon correlation functions.

ACKNOWLEDGMENTS

We thank Mike Buchoff for his 4-color operator code used for comparison to Ref. [7]. R.C.B. and C.R. acknowledge United States Department of Energy (DOE) Award No. DE-SC0015845. K.C. acknowl-

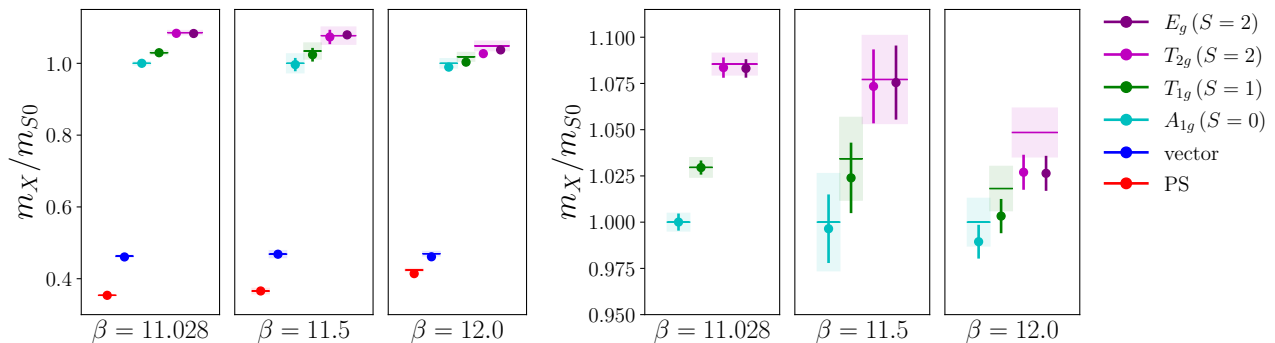


FIG. 9: Final results of the mesons and even-parity baryons (data points with error bars) using LapH and irreps compared to the spectrum results presented in Ref. [7] which use simple operators and Gaussian smearing (horizontal error bands). Masses, m_X , are in units of the spin-0 baryon mass as determined in Ref. [7], for each bare coupling, β . The right figure shows the same results, but zooming in to focus on the baryons. In the left figure, the errors are smaller than the points.

β	11.028	11.5	12.0
PS	1.8(4)	1.1(2)	1.01(5)
vector	2.0(2)	1.2(2)	1.03(2)
A_{1g} (0^+)	n/a	n/a	2.4(3)
T_{1g} (1^+)	n/a	n/a	2.07(5)
T_{2g} (2^+)	n/a	n/a	2.5(3)
E_g (2^+)	n/a	n/a	2.4(3)
A_{1u} (0^-)	n/a	n/a	n/a
T_{1u} (1^-)	n/a	n/a	2.4(2)
T_{2u} (2^-)	n/a	n/a	n/a
E_u (2^-)	n/a	n/a	n/a

TABLE VIII: Final results of second excited state hadron masses in lattice units for the three ensembles studied in this work, with “n/a” indicating combined fit not including this excited state.

edges support from the DOE through the Computational Sciences Graduate Fellowship (DOE CSGF) through grant No. DE-SC0019323 and also from the P.E.O. Scholar award. K.C. also thanks Luka Leskovec for guidance and support in setting up the LapH software. G.T.F. acknowledges support from DOE Award No. DE-SC0019061. A.D.G. is supported by SNSF grant No. 200021_17576. A.H. and E.T.N. acknowledge support by DOE Award No. DE-SC0010005. J.I. acknowledges support from ERC grant No. 101039756. G.D.K. acknowledges support from the DOE Award No. DE-SC0011640. The work of A.S.M. is supported in part by Lawrence Livermore National Security, LLC under Contract No. DE-AC52-07NA27344 with the DOE and by the Neutrino Theory Network Program Grant No. DE-AC02-07CHI11359 and DOE

Award No. DE-SC0020250. D.S. was supported by UK Research and Innovation Future Leader Fellowship MR/S015418/1 & MR/X015157/1 and STFC grants ST/T000988/1 & ST/X000699/1. P.V. acknowledges the support of the DOE under contract No. DE-AC52-07NA27344 (Lawrence Livermore National Laboratory, LLNL). We thank the LLNL Multiprogrammatic and Institutional Computing program for Grand Challenge supercomputing allocations. We also thank the Argonne Leadership Computing Facility (ALCF) for allocations through the INCITE program. ALCF is supported by DOE contract No. DE-AC02-06CH11357. Computations for this work were carried out in part on facilities of the USQCD Collaboration, which are funded by the Office of Science of the DOE, and on Boston University computers at the MGHPCC, in part funded by the National Science Foundation (award No. OCI-1229059). This research utilized the NVIDIA GPU accelerated Summit supercomputer at Oak Ridge Leadership Computing Facility at the Oak Ridge National Laboratory, which is supported by the DOE Office of Science under Contract No. DE-AC05-00OR22725.

Appendix A: Appendix

1. Tabulated isospin wavefunctions

Table IX shows all of the isospin $I = 0, 1, 2$ wavefunctions for SU(4) baryons. As described in Section II A 2, we constructed baryon operators with $I = S$, and for convenience, we used $I_z = I$.

Tableau				Label	I	I_z	orthonormal basis
1	2	3	4	TS	2	2	$uuuu$
					2	1	$\frac{1}{2}(u\bar{u}ud + u\bar{u}du + u\bar{d}uu + d\bar{u}uu)$
					2	0	$\frac{1}{\sqrt{6}}(u\bar{u}dd + u\bar{d}ud + d\bar{u}ud + d\bar{d}uu + d\bar{d}uu + u\bar{d}du)$
					2	-1	$\frac{1}{2}(u\bar{d}dd + d\bar{u}dd + d\bar{d}ud + d\bar{u}uu)$
					2	-2	$dddd$
1	3	4	MS ₁ ⁽¹⁾	1	1	$\frac{1}{\sqrt{2}}(ud - du)uu$	
2				1	0	$\frac{1}{2}(ud - du)(ud + du)$	
				1	-1	$\frac{1}{\sqrt{2}}(ud - du)dd$	
1	2	4	MS ₁ ⁽²⁾	1	1	$\sqrt{\frac{2}{3}}u\bar{u}du - \frac{1}{\sqrt{6}}(udu + duu)u$	
3				1	0	$\frac{1}{\sqrt{3}}u\bar{u}dd - \frac{1}{\sqrt{12}}(udu + duu)d + \frac{1}{\sqrt{12}}(udd + dud)u - \frac{1}{\sqrt{3}}dduu$	
				1	-1	$\frac{1}{\sqrt{6}}(udd + dud)d - \sqrt{\frac{2}{3}}ddud$	
1	2	3	MS ₁ ⁽³⁾	1	1	$\sqrt{\frac{3}{4}}(uuu)d - \frac{1}{\sqrt{12}}(uud + udu + duu)u$	
4				1	0	$\frac{1}{\sqrt{6}}(uud + udu + duu)d - \frac{1}{\sqrt{6}}(udd + dud + ddu)u$	
				1	-1	$\frac{1}{\sqrt{12}}(udd + dud + ddu)d - \sqrt{\frac{3}{4}}(ddd)u$	
1	3	MS ₀ ⁽¹⁾	0	0	$\frac{1}{2}(ud - du)(ud - du)$		
2	4						
1	2	MS ₀ ⁽²⁾	0	0	$\frac{1}{\sqrt{3}}(u\bar{u}dd + d\bar{d}uu) - \frac{1}{\sqrt{12}}(ud + du)(ud + du)$		
3	4						

TABLE IX: Irreducible representations of SU(2) isospin needed for SU(4) baryons determined from Clebsch-Gordon coefficients of four isospin-half fermions.

2. Tabulated irreps

In Table X, we tabulate the spin projections used in this work. Here we show only the irreps corresponding to $S = 0, 1, 2$, which, as shown in Table I, are A_1, T_1, E , and T_2 . The left-hand and right-hand tables correspond to even and odd parity irreps, respectively. See Section II A 3 for the descriptions of k and S_z .

The final column of each table shows the indices of the spin tensor χ which are nonzero, with coefficients providing the value of the tensor at those indices. For example, $0013 + 0233 - 2(0112 + 1223)$ corresponds to the spin tensor with $\chi_{0013} = \chi_{0233} = 1$ and $\chi_{0112} = \chi_{1223} = -2$, and zeros elsewhere. Note that the isospin wavefunctions for A_1 irreps and T_1 irreps are given as $I = 0$, $MS_0^{(2)}$ and $I = 1$, $MS_1^{(1)}$ from Table IX, respectively.

Note that the operators listed in Table X are not symmetrized, i.e. averaged over all permutations of the indices. It is unnecessary to symmetrized because only the total symmetric components of the flavor-spin wavefunction $\phi\chi$ contribute due to the symmetry of Equation 1, so we provide the simplest version of the operators in the table.

3. Non-intuitive combined fit cases

Most combined fits proceeded without issue according to the analysis procedure described above, but here, we explain each of the two types of special cases that come up. The first special case is when the combined fit parameters has significantly larger errors than the individual fits, for example in the E_g $\beta = 11.5$ correlation functions fits. Upon inspection of the fits, we find that only one- and two-state fits contributed to the model average of the single correlation fits, whereas three-state models dominated the combined fit model average. In this case, we remove the three-state models from the set of possible models and redid the combined fit, which yields parameters whose error was similar to the individual fits. In general, this case comes up when models dominating the single state fits are those with 2-states and a starting timeslice of 2, 3, or 4. The individual correlation function fits do not prefer to add another state because the reduction in χ^2 and inclusion of more timeslices do not compensate for the additional parameters of the model, whereas it does in the combined fit, at the expense of a much larger error. Of the 45 total combined fits per-

Λ	k	S_z	Nonzero elements of $\chi^{\Lambda,\lambda,k}$	Λ	k	S_z	Nonzero elements of $\chi^{\Lambda,\lambda,k}$
A_{1g}	1	0	0011 + 2233	A_{1u}	1	0	0011 - 2233
	2	0	0013 + 0233 - 2(0112 + 1223)		2	0	0013 - 0233 + 2(1223 - 0112)
	3	0	0123 + 2(0213)				
	4	0	0033 + 1122 + 4(0213)				
T_{1g}	1	1	0111 + 2333	T_{1u}	1	1	0111 - 2333
		0	0101 + 2323			0	0101 - 2323
		-1	0100 + 2322			-1	0100 - 2322
	2	1	0133 - 1213 + 1312		2	1	0133 + 1213 - 1312
		0	0123 - 0213 + 0312			0	0123 + 0213 - 0312
	-1	0122 - 0203 + 0302		-1	0122 + 0203 - 0302		
3	1	0311 + 0333 - 1211 + 1233 - 2(0113 + 1323)	3	1	0311 - 0333 - 1211 - 1233 + 2(1323 - 0113)		
	0	0103 + 0211 - 0233 - 0301 + 1322		0	0103 + 0211 + 0233 - 0301 - 1322		
	-1	0102 + 0201 - 0300 + 0322 + 1222 - 2(0223)		-1	0102 + 0201 - 0300 - 0322 - 1222 + 2(0223)		
4	1	0133 + 1213 + 1312 - 2(0313)	4	1	0113 + 0311 - 0333 - 1211 - 1323 + 2(1233)		
	0	0303 - 1212		0	0103 + 0233 - 1322 + 2(0301 - 0211)		
	-1	0122 + 0203 + 0302 - 2(0212)		-1	+3(0112 - 0323 + 1223)		
				-1	0201 - 0223 - 0300 - 1222 + 2(0322 - 0102)		
5	1	3(0311 + 0333 - 1211) + 4(0113 + 1323) - 7(1233)					
	0	2(0103 - 0233 + 1322) + 3(0301 - 0211)					
		+5(0112 + 0323 - 1223)					
	-1	3(0300 - 0201 - 1222) - 4(0223) + 7(0322 + 0102)					
E_g	1	0	0011 + 2233	E_u	1	0	0011 - 2233
		2	0000 + 1111 + 2222 + 3333			2	0000 + 1111 - 2222 - 3333
	2	0	0013 + 0112 + 0233 + 1223		2	0	0013 + 0112 - 0233 - 1223
		2	0002 + 0222 + 1113 + 1333			2	0002 + 1113 - 0222 - 1333
3	0	0033 + 1122 + 4(0123)					
	2	0022 + 1133					
T_{2g}	1	1	0133 + 1123	T_{2u}	1	1	0111 - 2333
		-1	0023 + 0122			-1	0001 - 2223
		2	0022 - 1133			2	0000 - 1111 - 2222 + 3333
2	1	0333 + 1112 + 3(0113 + 1233)	2	1	1112 - 0333 + 3(0113 - 1233)		
	-1	0003 + 1222 + 3(0012 + 0223)		-1	0003 - 1222 + 3(0012 - 0223)		
	2	0002 + 0222 - 1113 - 1333		2	0002 + 1333 - 0222 - 1113		
3	1	0111 + 2333					
	-1	0001 + 2223					
	2	0000 - 1111 + 2222 - 3333					

TABLE X: Irrep projections for positive-parity (left) and negative-parity (right) irreps, Λ , used in this work. See text for notation.

formed in this work, we resolve the issue as described here for 10 combined fits.

The other case where we have to stray from the original procedure occurred in the $\beta = 11.028$ odd-parity data sets for T_{1u} , T_{2u} , E_u . We find a very small t_{cut} in our pre-analysis data quality cuts, with values of $t_{\text{cut}} = 8, 4$, and 8 , respectively. We expect these correlation functions to have the worst signal because they are calculated on the coarsest lattice, where $N_{\text{vec}} = 32$ or more would be required to achieve a strong signal, but $N_{\text{vec}} = 24$ is used to reduce the computational cost. Nonetheless, we achieve satisfactory fits by increasing the cutoff time to $t_{\text{cut}} = 12$ which correspond to the value where the data was within

one standard deviation from zero, as opposed to eight standard deviations, as described in Section III B. We do not find that the results vary significantly from choosing different t_{cut} around $t_{\text{cut}} = 12$.

4. LapH computational costs

Note that the eigenvector solve time is not exactly linear in the number of eigenvectors, and depends on the algorithm used. We use the Arnoldi algorithm in the ARPACK++ matrix library

For the perambulator timing, note that, as described

in Section II B 1, computing an $N_{\text{vec}} \times N_{\text{vec}}$ perambulator, τ_{ij} requires N_{vec} inversions of the Dirac matrix, one for each source vector. Hence, the computation time is approximately proportional to the number of eigenvectors used at the source, $N_{\text{vec}}^{(\text{source})}$. Also, the inversion time depends on the fermion mass. This example considers the ensemble with $\beta = 12$ and $\kappa = 0.1475$, which corresponds to a relatively heavy fermion mass, with a pseudoscalar to vector mass ratio of $m_{\text{PS}}/m_V = 0.76$.

As described in Section II B 2, the meson correlation functions require N_{vec}^4 contractions, i.e. summation over indices i, i', j, j' running from 1 to N_{vec} . The baryon correlation function, in contrast requires $N_{\text{vec}}^{2N_c}$

The computational cost (complexity) of the tensor contractions in eigenvector indices for Eq. (19) is $O(N_{\text{vec}}^{N_c+1})$. The proof is as follows. In Eq. (19), $T_{ijkl}\tau_{ii'}$ involves $O(N_{\text{vec}}^5)$ complexity. And $\tilde{T}_{i'j'k'l'} \equiv T_{ijkl}\tau_{ii'}\tau_{jj'}\tau_{kk'}\tau_{ll'}$ involves four such consecutive operations and still gives $O(N_{\text{vec}}^5)$ computing complexity. The remaining contraction in Eq. (19), $T_{ijkl}\tilde{T}_{ijkl}$ is in $O(N_{\text{vec}}^4)$ complexity and it is a sub-leading amount of order, but one should note that it additionally scales with $N_{\text{operator}}^2 N_{\text{graph}}$ where N_{operator} is the number of operators in our variational basis and N_{graph} is the number of possible permutation in indices in the Wick contraction. In practice, N_{graph} can be much larger than N_{vec} , and therefore the last Wick contraction step becomes dominant in the computational cost. To reduce the factor of N_{graph} , further optimization with diagram consolidation and common sub-expression elimination [46] is in progress.

5. Review of projecting onto definite irreps

Please note that the following section can hold for spin projections in any $\text{SU}(N_c)$ theory by changing the number of indices on the spin tensors from $N_c = 4$.

Here, we review the method of calculating the irrep projected spin tensor, $\chi^{\Lambda\lambda,k}$ for a particular operator choice k of the d_Λ row of irrep Λ . For each of the d_Λ rows of the irrep, we will find K unique operator copies. Table XI tabulates the dimensions, d_Λ of each of the irreps, Λ . One can check these against the subduction table, Table I, to confirm that the dimensions match, i.e. $2J+1 = \sum d_{\Lambda_i}$ for each of the irreps Λ_i in the subduction of the continuum irrep J .

Λ	d_Λ	Λ	d_Λ
A_1	1	G_1	2
E	2	G_2	2
T_1	3	H	4
T_2	3		

TABLE XI: Dimensions, d_Λ of each of the irreps, Λ , corresponding to integer continuum spin (left) and half-integer continuum spin (right).

By the definition of being irreps, each of the K sets of d_Λ operators is a closed subspace under application of all elements of the group of rotations.

To compute the irrep projected spin tensor $\chi^{\Lambda\lambda,k}$ for lattice irrep Λ , row λ , and set k , we must determine the projection matrix, $P^{\Lambda,\lambda}$, and use

$$(\chi_i^{\Lambda,\lambda})_{\alpha\beta\sigma\delta} = \sum_j P_{ij}^{\Lambda,\lambda} (\chi_j)_{\alpha\beta\sigma\delta}, \quad (\text{A1})$$

where χ_j on the right-hand side is some convenient basis of spin tensors, which are most likely not irreps. In general, $P^{\Lambda,\lambda}$ has K linearly independent rows, so the projection produces K linearly independent spin tensors for irrep Λ and row λ . That is, $\chi^{\Lambda\lambda,k}$ is given by linearly independent combinations of $\chi_i^{\Lambda,\lambda}$ on the left hand side.

The matrix $P^{\Lambda,\lambda}$ is computed using the formula [29]

$$P_{ij}^{\Lambda,\lambda} = \frac{d_\Lambda}{g_{O_h^D}} \sum_{R \in O_h^D} \Gamma^\Lambda(R)_{\lambda,\lambda} W(R)_{ij}^{-1}, \quad (\text{A2})$$

where d_Λ is the dimension of the irrep, $g_{O_h^D}$ is the number of elements in the double point group, O_h^D , and sum is taken over all elements, R , of the group. The matrices $\Gamma^\Lambda(R)$ are the known set of $d_\Lambda \times d_\Lambda$ matrices which define the irrep. The matrices $W(R)$ are defined by how the spin tensor basis, χ_i transforms under each element, R , of the group. That is, $\chi_i \rightarrow W(R)_{ij} \chi_j$. The transformation rule is given by

$$(\chi_i)_{\alpha\beta\sigma\delta} \xrightarrow{R} \Lambda_{\frac{1}{2}}^{\alpha\alpha'} \Lambda_{\frac{1}{2}}^{\beta\beta'} \Lambda_{\frac{1}{2}}^{\sigma\sigma'} \Lambda_{\frac{1}{2}}^{\delta\delta'} (\chi_i)_{\alpha'\beta'\sigma'\delta'}, \quad (\text{A3})$$

where $\Lambda_{\frac{1}{2}} = \Lambda_{\frac{1}{2}}(R)$ is the usual Lorentz transformation for spinors under a rotation R . For example, the spin transformation for the octahedral group element corresponding to rotation of $\pi/2$ about the z -axis, the element called C_{4z} , is given by $\Lambda_{\frac{1}{2}}(C_{4z}) = \frac{1}{\sqrt{2}}(1 + \gamma_2\gamma_1)$.

The convenient basis of spin tensors, χ_i , depends on the flavor wavefunction. For example, in the positive parity irrep E_g , which corresponds to spin-2, we consider the totally symmetric flavor wavefunction $uuuu$. Using the notation from Equation 1, the flavor tensor $\phi = 1$ for $f_1 f_2 f_3 f_4 = (uuuu)$ and zero elsewhere. An $\text{SU}(4)$ baryon operator with this flavor wavefunction and arbitrary spin

is given by

$$\mathcal{O} = \sum_{a,b,c,d} \sum_{\alpha\beta\sigma\delta} \psi_{a\alpha} \psi_{b\beta} \psi_{c\sigma} \psi_{d\delta} \epsilon^{abcd} \phi_{uuuu} \chi_{\alpha\beta\sigma\delta}. \quad (\text{A4})$$

In this case, χ must be totally symmetric, so there are only $N = 35$ linearly independent choices for the spin indices. One choice of basis for the spin tensors is the 35 tensors having $\alpha \leq \beta \leq \sigma \leq \delta$.

-
- [1] G. D. Kribs and E. T. Neil, Review of strongly-coupled composite dark matter models and lattice simulations, *Int. J. Mod. Phys. A* **31**, 1643004 (2016), arXiv:1604.04627 [hep-ph].
- [2] J. M. Cline, Dark atoms and composite dark matter, *SciPost Phys. Lect. Notes* **52**, 1 (2022), arXiv:2108.10314 [hep-ph].
- [3] P. Asadi *et al.*, Early-Universe Model Building, (2022), arXiv:2203.06680 [hep-ph].
- [4] G. D. Kribs, T. S. Roy, J. Terning, and K. M. Zurek, Quirky Composite Dark Matter, *Phys. Rev. D* **81**, 095001 (2010), arXiv:0909.2034 [hep-ph].
- [5] M. R. Buckley and E. T. Neil, Thermal dark matter from a confining sector, *Phys. Rev. D* **87**, 043510 (2013), arXiv:1209.6054 [hep-ph].
- [6] T. Appelquist, R. C. Brower, M. I. Buchoff, M. Cheng, S. D. Cohen, G. T. Fleming, J. Kiskis, M. F. Lin, E. T. Neil, J. C. Osborn, C. Rebbi, D. Schaich, C. Schroeder, S. N. Syritsyn, G. Voronov, P. Vranas, and J. Wasem (Lattice Strong Dynamics Collaboration), Lattice Calculation of Composite Dark Matter Form Factors, *Phys. Rev. D* **88**, 014502 (2013), arXiv:1301.1693 [hep-ph].
- [7] T. Appelquist, E. Berkowitz, R. C. Brower, M. I. Buchoff, G. T. Fleming, J. Kiskis, G. D. Kribs, M. F. Lin, E. T. Neil, J. C. Osborn, C. Rebbi, E. Rinaldi, D. Schaich, C. Schroeder, S. Syritsyn, G. Voronov, P. Vranas, E. Weinberg, and O. Witzel (Lattice Strong Dynamics Collaboration), Composite bosonic baryon dark matter on the lattice: SU(4) baryon spectrum and the effective Higgs interaction, *Phys. Rev. D* **89**, 094508 (2014), arXiv:1402.6656 [hep-lat].
- [8] O. Antipin, M. Redi, and A. Strumia, Dynamical generation of the weak and Dark Matter scales from strong interactions, *JHEP* **01**, 157, arXiv:1410.1817 [hep-ph].
- [9] T. Appelquist, R. C. Brower, M. I. Buchoff, G. T. Fleming, X.-Y. Jin, J. Kiskis, G. D. Kribs, E. T. Neil, J. C. Osborn, C. Rebbi, E. Rinaldi, D. Schaich, C. Schroeder, S. Syritsyn, P. Vranas, E. Weinberg, and O. Witzel (Lattice Strong Dynamics Collaboration), Stealth Dark Matter: Dark scalar baryons through the Higgs portal, *Phys. Rev. D* **92**, 075030 (2015), arXiv:1503.04203 [hep-ph].
- [10] O. Antipin, M. Redi, A. Strumia, and E. Vigiani, Accidental Composite Dark Matter, *JHEP* **07**, 039, arXiv:1503.08749 [hep-ph].
- [11] J. M. Cline, W. Huang, and G. D. Moore, Challenges for models with composite states, *Phys. Rev. D* **94**, 055029 (2016), arXiv:1607.07865 [hep-ph].
- [12] A. Mitridate, M. Redi, J. Smirnov, and A. Strumia, Dark Matter as a weakly coupled Dark Baryon, *JHEP* **10**, 210, arXiv:1707.05380 [hep-ph].
- [13] S. J. Lonsdale, M. Schroor, and R. R. Volkas, Asymmetric Dark Matter and the hadronic spectra of hidden QCD, *Phys. Rev. D* **96**, 055027 (2017), arXiv:1704.05213 [hep-ph].
- [14] N. A. Dondi, F. Sannino, and J. Smirnov, Thermal history of composite dark matter, *Phys. Rev. D* **101**, 103010 (2020), arXiv:1905.08810 [hep-ph].
- [15] L. Morrison, S. Profumo, and D. J. Robinson, Large N -nightmare Dark Matter, *JCAP* **05**, 058, arXiv:2010.03586 [hep-ph].
- [16] T. Appelquist, E. Berkowitz, R. C. Brower, M. I. Buchoff, G. T. Fleming, X.-Y. Jin, J. Kiskis, G. D. Kribs, E. T. Neil, J. C. Osborn, C. Rebbi, E. Rinaldi, D. Schaich, C. Schroeder, S. Syritsyn, P. Vranas, E. Weinberg, and O. Witzel (Lattice Strong Dynamics Collaboration), Detecting Stealth Dark Matter Directly through Electromagnetic Polarizability, *Phys. Rev. Lett.* **115**, 171803 (2015), arXiv:1503.04205 [hep-ph].
- [17] T. Schaich (Lattice Strong Dynamics Collaboration), Stealth dark matter and gravitational waves, *PoS LATTICE2019*, 068 (2020), arXiv:2002.00187 [hep-lat].
- [18] R. C. Brower, K. Cushman, G. T. Fleming, A. Gasbarro, A. Hasenfratz, X. Y. Jin, G. D. Kribs, E. T. Neil, J. C. Osborn, C. Rebbi, E. Rinaldi, D. Schaich, P. Vranas, and O. Witzel (Lattice Strong Dynamics Collaboration), Stealth dark matter confinement transition and gravitational waves, *Phys. Rev. D* **103**, 014505 (2021), arXiv:2006.16429 [hep-lat].
- [19] F. Springer and D. Schaich (Lattice Strong Dynamics Collaboration), Progress applying density of states for gravitational waves, *EPJ Web Conf.* **274**, 08008 (2022), arXiv:2212.09199 [hep-lat].
- [20] K. K. Cushman and C. Culver (Lattice Strong Dynamics Collaboration), Progress Toward Stealth Dark Matter Scattering, *PoS LATTICE2022*, 208 (2023).
- [21] M. Luscher, Volume Dependence of the Energy Spectrum in Massive Quantum Field Theories. 2. Scattering States, *Commun. Math. Phys.* **105**, 153 (1986).
- [22] M. Luscher, Two particle states on a torus and their relation to the scattering matrix, *Nucl. Phys. B* **354**, 531 (1991).
- [23] M. T. Hansen, R. A. Briceño, R. G. Edwards, C. E. Thomas, and D. J. Wilson, Energy-dependent $\pi^+\pi^+\pi^+$ scattering amplitude from QCD, *Physical Review Letters* **126**, 10.1103/physrevlett.126.012001 (2021).
- [24] B. Hörz, D. Howarth, E. Rinaldi, A. Hanlon, C. C. Chang, C. Körber, E. Berkowitz, J. Bulava, M. A. Clark, W. T. Lee, C. Morningstar, A. Nicholson, P. Vranas, and A. Walker-Loud, Two-nucleon s -wave interactions at the SU(3) flavor-symmetric point with $m_{ud} \simeq m_s^{\text{phys}}$: A first lattice QCD calculation with the stochastic laplacian heaviside method, *Physical Review C* **103**, 10.1103/physrevc.103.014003 (2021).
- [25] J. Bulava *et al.* (Baryon Scattering Collaboration), Lattice QCD study of $\pi\Sigma - \bar{K}N$ scattering and the $\Lambda(1405)$ resonance, (2023), arXiv:2307.13471 [hep-lat].
- [26] M. Peardon, J. Bulava, J. Foley, C. Morningstar, J. Dudek, R. G. Edwards, B. Joó, H.-W. Lin, D. G.

- Richards, and K. J. Juge, Novel quark-field creation operator construction for hadronic physics in lattice QCD, *Physical Review D* **80**, 10.1103/physrevd.80.054506 (2009).
- [27] C. Morningstar, J. Bulava, J. Foley, K. J. Juge, D. Lenkner, M. Peardon, and C. H. Wong, Improved stochastic estimation of quark propagation with laplacian heaviside smearing in lattice QCD, *Physical Review D* **83**, 10.1103/physrevd.83.114505 (2011).
- [28] R. C. Johnson, Angular momentum on a lattice, *Phys. Lett. B* **114**, 147 (1982).
- [29] S. Basak, R. G. Edwards, G. T. Fleming, U. M. Heller, C. Morningstar, D. Richards, I. Sato, and S. Wallace, Group-theoretical construction of extended baryon operators in lattice QCD, *Phys. Rev. D* **72**, 094506 (2005), arXiv:hep-lat/0506029.
- [30] C. Morningstar, J. Bulava, A. D. Hanlon, B. Hörz, D. Mohler, A. Nicholson, S. Skinner, and A. Walker-Loud, Progress on Meson-Baryon Scattering, *PoS LATTICE2021*, 170 (2022), arXiv:2111.07755 [hep-lat].
- [31] G. Silvi *et al.*, P -wave nucleon-pion scattering amplitude in the $\Delta(1232)$ channel from lattice QCD, *Phys. Rev. D* **103**, 094508 (2021), arXiv:2101.00689 [hep-lat].
- [32] W. I. Jay and E. T. Neil, Bayesian model averaging for analysis of lattice field theory results, *Physical Review D* **103**, 10.1103/physrevd.103.114502 (2021).
- [33] E. T. Neil and J. W. Sitison, Improved information criteria for Bayesian model averaging in lattice field theory, (2022), arXiv:2208.14983 [stat.ME].
- [34] M. L. Wagman and M. J. Savage, Statistics of baryon correlation functions in lattice QCD, *Phys. Rev. D* **96**, 114508 (2017), arXiv:1611.07643 [hep-lat].
- [35] G. Parisi, The Strategy for Computing the Hadronic Mass Spectrum, *Phys. Rept.* **103**, 203 (1984).
- [36] G. P. Lepage, The Analysis of Algorithms for Lattice Field Theory, in *Theoretical Advanced Study Institute in Elementary Particle Physics* (1989).
- [37] S. Basak, R. Edwards, R. Fiebig, G. T. Fleming, U. M. Heller, C. Morningstar, D. Richards, I. Sato, and S. Wallace (Lattice Hadron Physics Collaboration), Baryonic sources using irreducible representations of the double-covered octahedral group, *Nucl. Phys. B Proc. Suppl.* **140**, 281 (2005), arXiv:hep-lat/0409080.
- [38] S. Basak, R. Edwards, G. T. Fleming, U. M. Heller, C. Morningstar, D. Richards, I. Sato, and S. J. Wallace (Lattice Hadron Physics Collaboration), Clebsch-Gordan construction of lattice interpolating fields for excited baryons, *Phys. Rev. D* **72**, 074501 (2005), arXiv:hep-lat/0508018.
- [39] M. Cè, M. García Vera, L. Giusti, and S. Schaefer, The topological susceptibility in the large- N limit of $SU(N)$ Yang–Mills theory, *Phys. Lett. B* **762**, 232 (2016), arXiv:1607.05939.
- [40] T. DeGrand, Simple chromatic properties of gradient flow, *Phys. Rev. D* **95**, 114512 (2017), arXiv:1701.00793.
- [41] R. G. Edwards and B. Joo (SciDAC, LHPC, UKQCD), The Chroma software system for lattice QCD, *Nucl. Phys. B Proc. Suppl.* **140**, 832 (2005), arXiv:hep-lat/0409003.
- [42] O. Ledoit and M. Wolf, A well-conditioned estimator for large-dimensional covariance matrices, *Journal of Multivariate Analysis* **88**, 365 (2004).
- [43] E. Rinaldi, S. Syritsyn, M. L. Wagman, M. I. Buchoff, C. Schroeder, and J. Wasem, Lattice QCD determination of neutron-antineutron matrix elements with physical quark masses, *Phys. Rev. D* **99**, 074510 (2019), arXiv:1901.07519 [hep-lat].
- [44] R. C. Brower, E. Owen, C. Rebbi, C. Culver, D. Schaich, K. K. Cushman, G. T. Fleming, A. Gasbarro, A. Hasenfratz, E. T. Neil, J. Ingoldby, X. Y. Jin, J. C. Osborn, E. Rinaldi, P. Vranas, E. Weinberg, and O. Witzel (Lattice Strong Dynamics Collaboration), Light Scalar Meson and Decay Constant in $SU(3)$ Gauge Theory with Eight Dynamical Flavors, (2023), arXiv:2306.06095 [hep-lat].
- [45] S. Amarasinghe, R. Baghdadi, Z. Davoudi, W. Detmold, M. Illa, A. Parreno, A. V. Pochinsky, P. E. Shanahan, and M. L. Wagman, Variational study of two-nucleon systems with lattice QCD, *Phys. Rev. D* **107**, 094508 (2023), arXiv:2108.10835 [hep-lat].
- [46] B. Hörz and A. Hanlon, Two- and three-pion finite-volume spectra at maximal isospin from lattice QCD, *Phys. Rev. Lett.* **123**, 142002 (2019), arXiv:1905.04277 [hep-lat].